Increasing Cancer Therapy Efficiency through Targeting and Localized Light Activation

Yuqi Yang,[†,§] Shizhen Chen,[†,§] Lianhua Liu,[†] Sha Li,[†] Qingbin Zeng,[†] Xiuchao Zhao,[†] Haidong Li,[†] Zhiying Zhang,[†] Louis-S. Bouchard,[‡] Maili Liu,[†] and Xin Zhou*[,†]
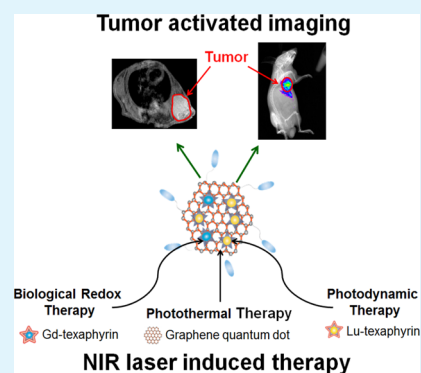
[†]Key Laboratory of Magnetic Resonance in Biological Systems, State Key Laboratory of Magnetic Resonance and Atomic and Molecular Physics, National Center for Magnetic Resonance in Wuhan, Wuhan Institute of Physics and Mathematics, Chinese Academy of Sciences, Wuhan 430071, P. R. China

[‡]Department of Chemistry and Biochemistry and Department of Bioengineering, California NanoSystems Institute, The Molecular Biology Institute, Jonsson Comprehensive Cancer Center, University of California, Los Angeles, California 90095, United States

Ⓢ *Supporting Information*

ABSTRACT: Currently, the potential of cancer therapy is compromised by a variety of problems related to tumor specificity, drug access, and limited efficacy. We report a novel approach to improve the effectiveness of cancer treatment utilizing a light-responsive nanoconstruct. Effectiveness is increased by enhancing drug absorption through heating and the production of free radicals. Treatment specificity is increased through chemical targeting of the nanoconstruct and localization of light delivery to the tumor. When reaching the tumor, magnetic resonance imaging is enhanced and near-infrared fluorescence is activated upon drug release, making it possible to visualize the localized treatment at both the tissue and cellular levels. This dual-modality imaging nanoconstruct enables the synergistic treatment and observable evaluation of solid tumors with dramatically improved efficacy, giving rise to a promising new approach for cancer therapy and evaluation.

KEYWORDS: *photodynamic therapy, biological redox therapy, photothermal therapy, graphene quantum dots, dual-modality imaging*

INTRODUCTION

Current methods to treat cancer often involve intrusive processes such as the application of chemotherapy, tumor resection surgery, or radiation therapy.[1] Several potential cancer therapies take advantage of the free radical imbalance within cancer cells.[2] In this work, we employed two different methods for the production of free radicals. The first method is photodynamic therapy (PDT).[3] PDT involves the selective uptake of a photosensitizer (PS) that inhibits cancer cell growth by generating reactive oxygen species (ROS) after irradiation with light at a specific wavelength.[4,5] PDT has been successfully used in a variety of treatments, such as ocular vascular hyperplasia, skin cancers, and lung cancers.[6−8] The use of lutetium(III) texaphyrin (Lu-TP) for PDT[9] is motivated by its strong absorption in the spectral region >700 nm, where tissues are more transparent to light. The second method is biological redox therapy (BRT). Gadolinium(III) texaphyrin (Gd-TP) is a tumor-selective redox drug that interacts with many intracellular-reducing metabolites.[10] New synergistic treatment modalities that combine PDT with other therapies, such as chemotherapy, radiation therapy, surgery, immunotherapy, and photothermal therapy (PTT), hold promise for enhancing anticancer efficacy.[11−17] The combination of BRT with PDT has not been reported in vivo so far. Gd-TP can induce the depletion of intracellular-reducing metabolites and bioenergetic disruption, upregulate metallothionein-related genes, and break
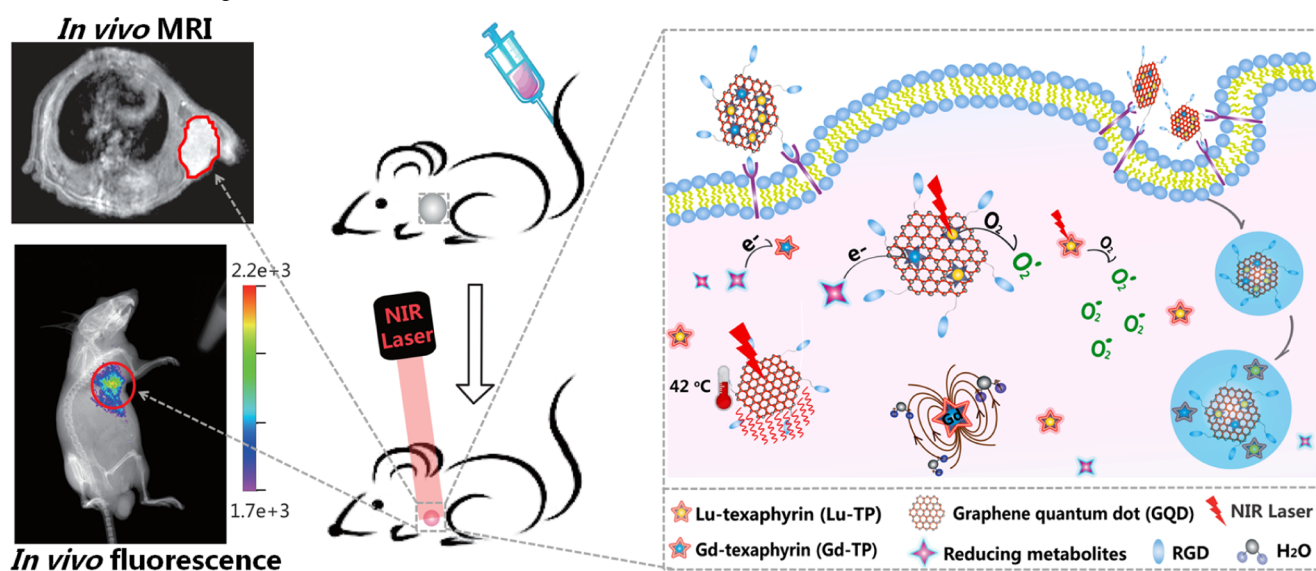
the cellular antioxidant system, which protects cells against oxidative damage from ROS.[10] Hence, the introduction of Gd-TP may cooperate with Lu-TP-induced ROS generation and further trigger tumor response to PDT.

To improve the water solubility and the specific targeting of drugs, various nanocarriers have been developed.[18] Graphene quantum dots (GQDs) offer a suitable size, excellent water solubility, stability, and autofluorescence.[19] GQDs have a polyaromatic structure featuring a high surface area that enables the simultaneous loading of Lu-TP and Gd-TP drugs via π−π stacking. A cyclic peptide, c(RGDyK) (cyclo(Arg-Gly-Asp-D-Phe-Lys)), is conjugated to GQDs to enhance the selectivity. c(RGDyK) has a high affinity for the integrin $\alpha_v\beta_3$,[20] which is overexpressed by many solid tumor cells. Moreover, by using GQDs as a photothermal agent, we are able to achieve mild heating of only 43 °C with low-power near-infrared (NIR) light. It has been demonstrated that PTT of ∼43 °C by laser-irradiated FeCo/graphitic nanoparticles could enhance the intracellular delivery of the chemotherapy drug for improved cancer cell killing.[21] In this work, the GQD delivery offers dramatically increased intracellular shuttling of Lu-TP and Gd-

Scheme 1. Description of Nanoconstruct To Deliver Cancer Treatment via Biological Redox-Enhanced PDT Combined with Photothermal Heating[a]

[a]The water insoluble PS Lu-TP and redox drug Gd-TP are loaded onto GQD-RGD through $\pi-\pi$ stacking. The nanoconstruct could be selectively endocytosed by A549 cells. Upon NIR irradiation, the GQDs heat the cells mildly, thereby promoting endocytosis of the nanoconstruct. Furthermore, the enriched paramagnetic Gd(III) in the tumor and the recovered fluorescence from the released drugs make it possible to assess the therapeutic efficiency by MRI and fluorescence imaging.
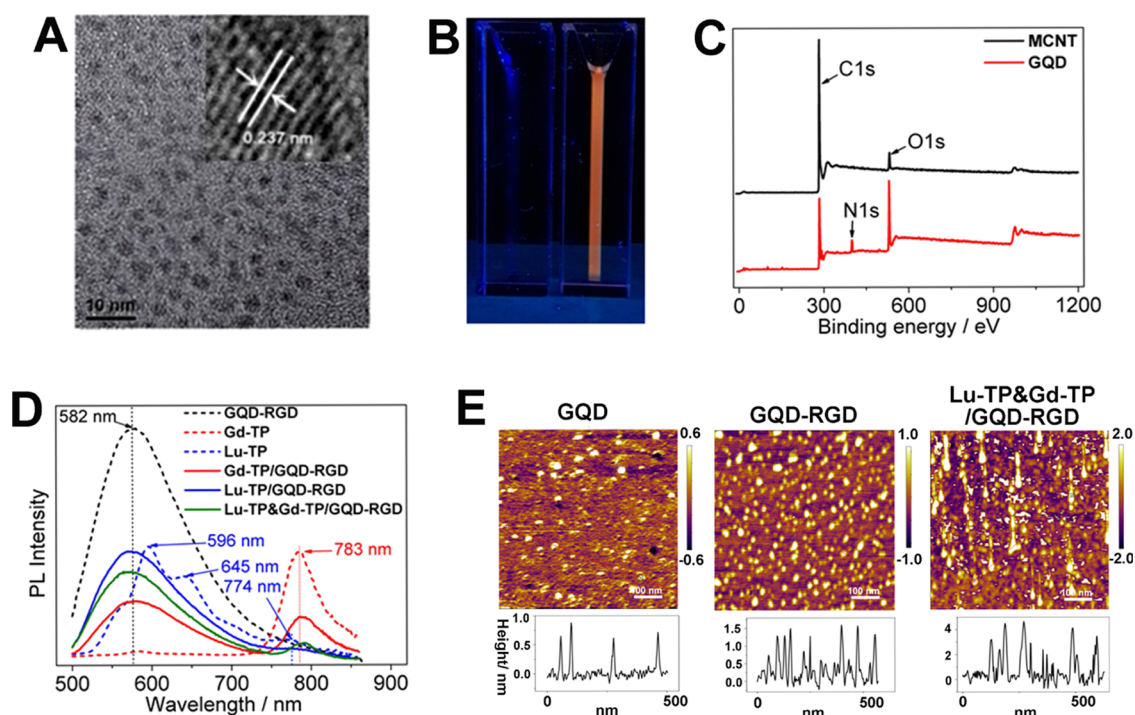

Figure 1. (A) TEM image of GQDs shows their uniform size distribution. Inset of (A): HRTEM of GQDs. (B) The GQD aqueous solution emitted orange fluorescence under UV lamp irradiation (365 nm). (C) XPS spectra of GQDs (red) and MCNTs (black). (D) Photoluminescence spectra of GQDs (dashed black line), Gd-TP (dashed red line), Lu-TP (dashed blue line), Gd-TP/GQD (solid red line), Lu-TP/GQD (solid blue line), and Lu-TP&Gd-TP/GQD (solid green line). (E) AFM images and height distribution of GQD, GQD-RGD, and Lu-TP&Gd-TP/GQD-RGD.

TP drugs, largely enhancing the light-induced cancer cell killing efficiency.

Multimodal imaging based on complementary detection principles has broad clinical applications and can improve diagnostic accuracy.[22] Paramagnetic Gd-TP enhances magnetic resonance imaging (MRI) contrast in regions where the drug is delivered,[23] which can greatly shorten the relaxation times of water protons. Meanwhile, the nanoconstruct enables the Lu-TP and Gd-TP drugs to exhibit a fluorescence "turn-on" signal when it enters a tumor. After the Lu-TP and Gd-TP drugs are loaded onto the GQDs to form the nanoconstruct, their fluorescence is quenched. On exposure to the microenviron-
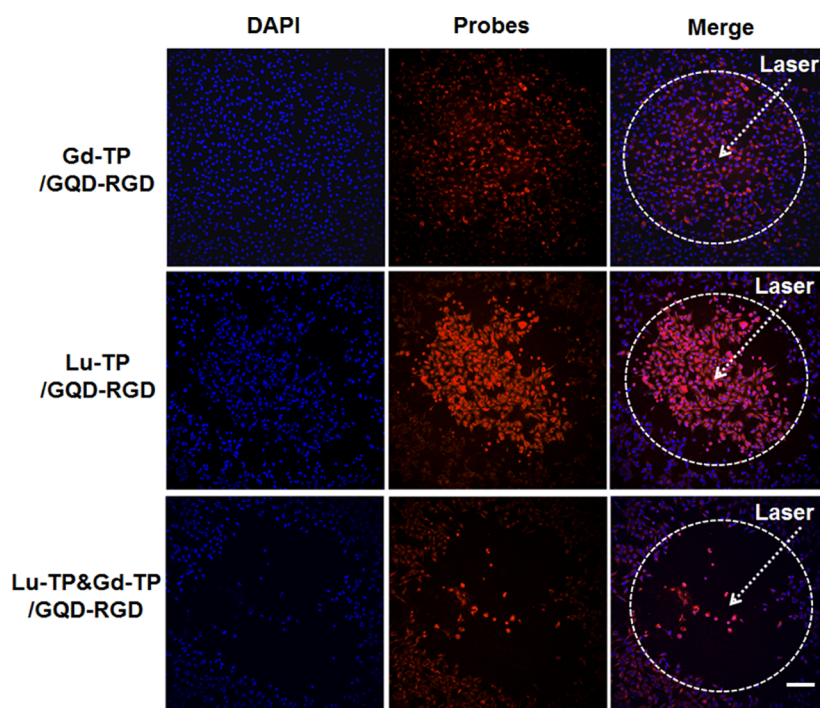
Figure 2. In vitro PDT effect investigated by confocal laser scanning microscopy (CLSM). Lung cancer cells (A549) were incubated with Gd-TP/GQD, Lu-TP/GQD, and Lu-TP&Gd-TP/GQD-RGD for 4 h. After medium exchange, cells were irradiated with a 765 nm laser at a power density of 50 mW/cm^2 for 4 min (12 J/cm^2). A mask was employed to confine the laser beam to a circular region with a diameter of 1 mm (as indicated by the white dashed circles). Scale bar, 100 μm.

ments within a tumor, the loaded drugs are released from the GQD-RGD sheets due to changes in pH and hydrophobicity, resulting in fluorescence recovery. By employing dual-modality imaging upon activation by the tumor microenvironment, the nanoconstruct allows the cancer therapy to be more easily assessed.

The nanoconstruct, Lu-TP&Gd-TP/GQD-RGD, uses a PTT-generating GQD as the drug delivery vehicle. The GQD is conjugated to the RGD peptide for cancer cell targeting. GQD-RGD is loaded with the PDT drug Lu-TP and the BRT drug Gd-TP. Because of the synergistic therapy of BRT, PDT, and PTT (Scheme 1), the nanoconstruct efficiently suppresses tumor growth under low-power light at 765 nm. This system enables the assessment of the cancer therapy by dual-modality enhanced imaging.

■ RESULTS AND DISCUSSION

Preparation of Lu-TP&Gd-TP/GQD-RGD. GQDs with a mean diameter of 6 nm (Figure 1A) were prepared by the following steps: multiwalled carbon nanotubes (MWCNTs) were oxidized in a mixture of concentrated acid and then cut into small pieces by a microwave-assisted hydrothermal route. The high-resolution transmission electron microscopy (HRTEM) image (inset of Figure 1A) indicates the high crystallinity of the GQDs, with a lattice parameter of 0.237 nm, corresponding to the (1120) lattice fringes of graphene. This reveals the transformation of amorphous oxidized debris to highly crystalline GQDs after the hydrothermal treatment. The GQD edges seem to be predominantly parallel to the zigzag orientation. The GQD aqueous solution emitted bright orange fluorescence under a 365 nm UV light (Figure 1B), most likely because there is a high concentration of zigzag sites on the edges.[24] Their high quantum yield (21.6% against that of

Rhodamine 6G) may result from energy level quantization due to their uniform size distribution, or from the dimethylamine introduced via the decomposition of dimethylformamide (DMF), as dimethylamine has a strong electron-donating interaction with sp^2-hybridized GQDs.[25] A detailed analysis of the XPS spectra (Figure 1C) certified the solvothermal doping of the GQDs with nitrogen. The targeting molecular RGD was linked to the GQDs by a bridge of poly(ethylene glycol) (PEG) (Figure S-1). The RGD component was detected to be 1.06% (0.017 μmol/mg) in the vehicle GQD-RGD. Figure S-2 shows the very similar fluorescence emission of the GQDs and GQD-RGD, which exhibits a maximum emission at ~582 nm under a laser wavelength of 490 nm. Texaphyrin was synthesized by a six-step reaction, and the structure was confirmed by ^{1}H NMR (Figure S-3) and high-resolution mass spectroscopy (Figure S-4). Then, the chelates of texaphyrin with gadolinium (Figure S-5) and lutetium (Figure S-6) were characterized by mass spectroscopy. The insoluble PS Lu-TP and BRT drug Gd-TP were immobilized onto GQD-RGD via simple stirring in a dimethyl sulfoxide (DMSO)/water mixture. DMSO was removed by dialyzing against deionized (DI) water. The formed nanoconstruct was concentrated by ultrafiltration, and named Lu-TP&Gd-TP/GQD-RGD. UV−vis spectra of the obtained aqueous solution showed typical peaks of Lu-TP and Gd-TP (Figure S-7), suggesting the successful loading of the water insoluble drugs on GQD-RGD through π−π stacking and hydrophobic effects. The designed probe could be well dispersed in water when the weight ratio is less than 36% ($m_{\text{Lu-TP&Gd-TP}}/m_{\text{GQD-RGD}}$). We suppose that the increased hydrophobicity may cause aggregation at higher metal-texaporphyrin contents. The dispersion status was also investigated, and the results showed that Lu-TP&Gd-TP/GQD-RGD (30% weight ratio) could stably disperse in 1 mL of
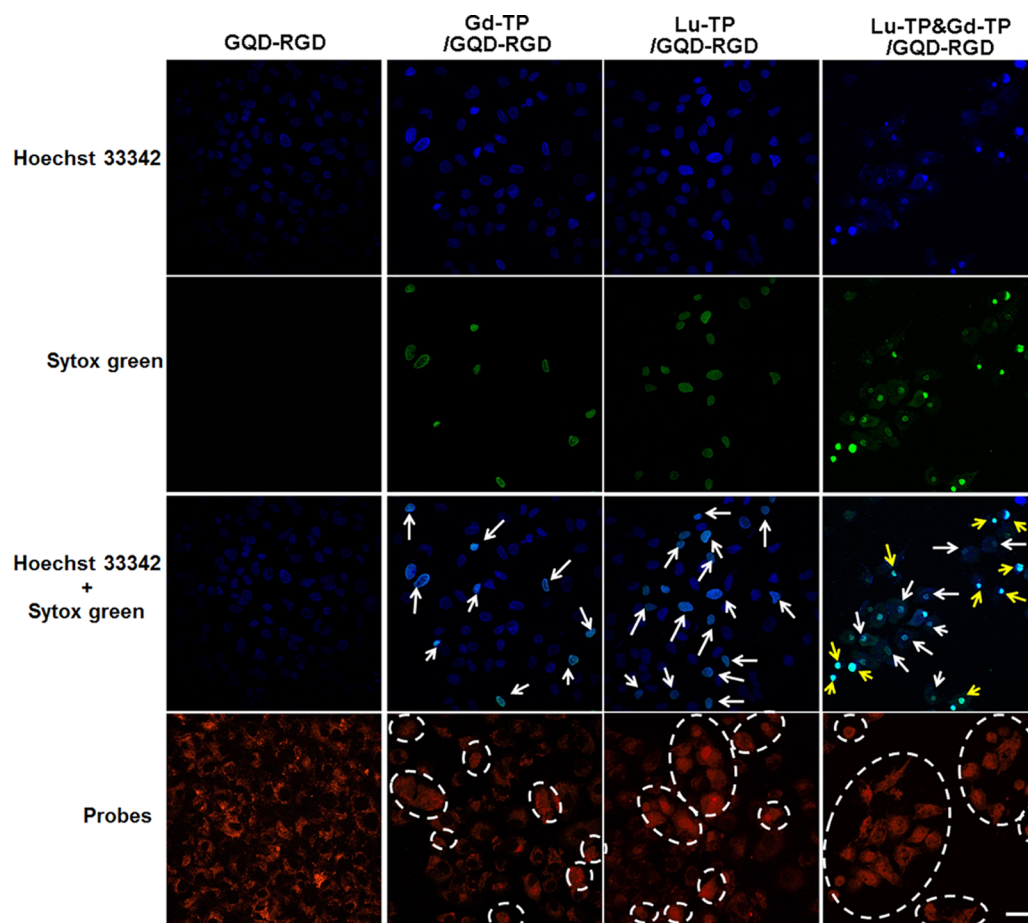
Figure 3. Measurement of apoptosis after PDT. Ten hours after 50 mW/cm² laser-induced PDT, A549 cells were stained with Hoechst 33342 (blue) and sytox green (green). Scale bar, 50 μm.

water, PBS, cell medium Dulbecco's modified Eagle's medium (DMEM), or 10% serum for over a month when stored at 4 °C (Figure S-8).

Characterization. We studied the interaction between the drugs and vehicles by recording their typical fluorescence emission. Figure 1D indicates that GQD-RGD exhibited a maximum emission of ∼582 nm upon excitation at 490 nm. Gd-TP showed two peaks at 597 and 642 nm, as well as a small peak at 783 nm. Lu-TP showed a typical peak at 774 nm. The emission peak of GQD-RGD shifted toward the NIR region as the excitation wavelength varied from 430 to 560 nm, whereas the two drugs sustained their characteristic peak as the excitation wavelength increased (Figure S-9). After drug loading, the fluorescence of GQD-RGD, Gd-TP, and Lu-TP were all partly quenched (Figure 1D). Interestingly, the fluorescence intensity of Gd-TP/GQD-RGD at 582 nm was stronger than that of Lu-TP/GQD-RGD, possibly because of the fluorescence overlap of Gd-TP and GQD-RGD. The representative emission peaks of Gd-TP (783 nm) and Lu-TP (774 nm) were still observed after loading onto GQD-RGD independently. Whereas, when the two drugs were loaded onto GQD-RGD together, the small peak at 774 nm for Lu-TP could not be monitored because it is covered by the stronger fluorescence emission of Gd-TP at around 783 nm. Additional confirming evidence was obtained by AFM (Figure 1E). Free GQDs exhibited a uniform height of 0.71 nm, indicating a single layer structure. Whereas the thickness increased to 1.46 nm after modification, this is due to the attachment of PEG and

its wrapping and folding on the two planes of the GQDs. The height continuously increased to 4.01 nm after drug loading, indicating the immobilization of a larger amount of Lu-TP and Gd-TP onto the GQD-RGD sheets.

On the basis of the ability to generate ROS or react with some biological substrates under laser irradiation, a PS can selectively damage irradiated cancer cells and leave unexposed healthy cells unaffected. We investigated the singlet oxygen ($^1O_2$) generation of Lu-TP&Gd-TP/GQD-RGD under 765 nm irradiation. The results showed that the generated $^1O_2$ species by Lu-TP/GQD-RGD and Lu-TP&Gd-TP/GQD-RGD were obviously larger than that of Gd-TP/GQD-RGD (Figure S-10). According to Mody et al.,[26] the photosensitization and singlet oxygen production induced by Lu-TP is much higher than that of Gd-TP. In view of the above results, the generation of $^1O_2$ by Lu-TP&Gd-TP/GQD-RGD is likely caused by the loaded Lu-TP.

Increasing Therapy Efficiency in Living Cells. The development of PDT has been restricted because the rapid attenuation of light in tissue causes long irradiation times. In this work, we overcome this limitation by introducing a redox drug, Gd-TP. Gd-TP can accept electrons from various cellular reducing metabolites and form ROS, which results in enhanced cellular redox stress. Cancer cells may be more susceptible to oxidative damage from PDT if the two drugs cooperate well with each other. Thus, a weaker light with a shorter irradiation time may lead to a more efficient PDT. The results in Figure 2 confirm this hypothesis. Human lung cancer cells (A549) were
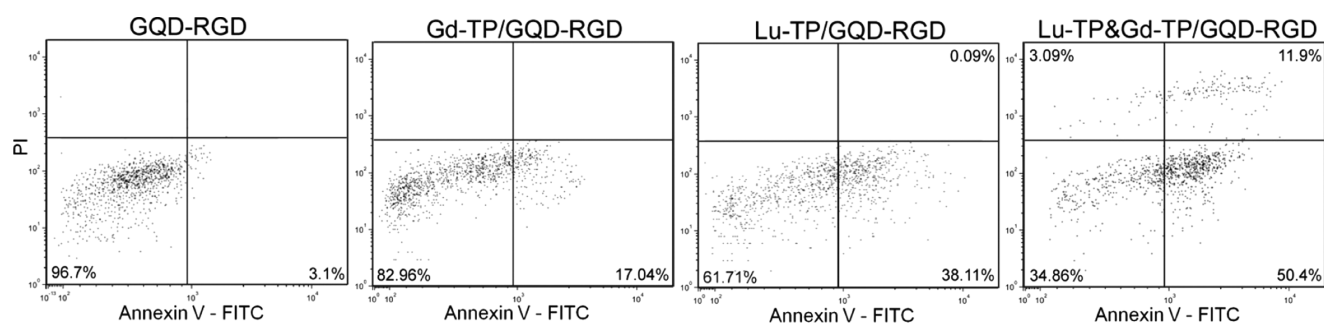
Figure 4. Annexin V-FITC/PI apoptosis assay measured the apoptotic and necrotic rate of A549 cells 10 h after laser treatment.
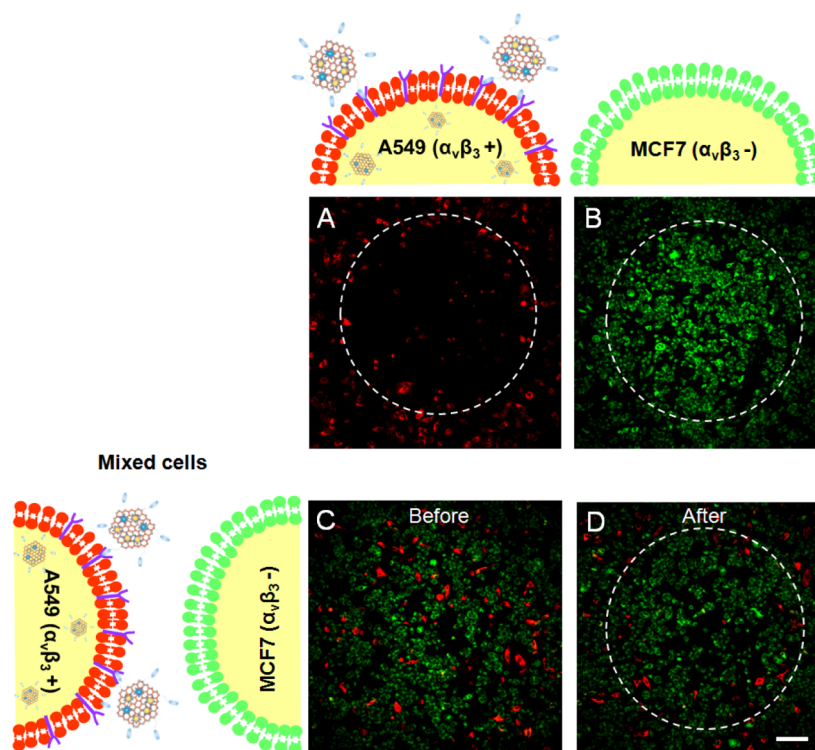

Figure 5. Selectivity of Lu-TP&Gd-TP/GQD-RGD. Red-labeled lung cancer A549 cells (A, $\alpha_v\beta_3$+) and green-labeled breast cancer MCF7 cells (B, $\alpha_v\beta_3$-) were treated with Lu-TP&Gd-TP/GQD-RGD for 30 min. Cells were irradiated with a 765 nm laser at a power density of 50 mW/cm^2 for 4 min (12 J/cm^2). CLSM images of a mixture of red-labeled A549 cells and green-labeled MCF7 cells are shown (C) before and (D) after laser treatment. In the irradiated region after culture for 24 h, A549 cells (red) were depleted, whereas MCF7 cells (green) remained alive on the substrate. Scale bar, 100 μm.

incubated with the three probes, Gd-TP/GQD-RGD, Lu-TP/GQD-RGD, and Lu-TP&Gd-TP/GQD-RGD respectively, and then irradiated with a 765 nm laser at a low-power density of 50 mW/cm^2 for 4 min. Gd-TP/GQD-RGD localized in the cytoplasm and perinuclear region of the A549 cells (Figure S-11). Both the light-treated (Figure S-11) and untreated cells (Figure S-12) attached well and were spindle shaped, illustrating that the Gd-TP/GQD-RGD incubated cells did not show an obvious response to light treatment. After irradiation, the Lu-TP/GQD-RGD treated cells located in the laser-irradiated area were found to be loosely attached, rounded, and randomly oriented (Figure S-11, yellow cycles). Meanwhile, fluorescence was observed in the nucleus of some irradiated cells (Figure S-11, green arrows), indicating damage of the nuclear membrane by PDT. Only a small amount of Lu-TP&Gd-TP/GQD-RGD treated cells were observed within the laser-irradiated area (Figure 2), because these adhered cells were killed and separated from the substrates by redox

perturbations together with the PDT process. Cells remained attached in the region outside the laser footprint (Figure S-12), illustrating the low dark toxicity of the probe. The above results confirm that the PDT response from Lu-TP is accelerated by the addition of Gd-TP.

To better demonstrate the enhancement of Gd-TP to Lu-TP induced PDT, a live/dead cell assay was performed to understand the cytotoxicity, apoptosis, and/or necrosis. A549 cells treated with GQD-RGD were viable (Hoechst 33342+/sytox green) after irradiation. Whereas, apoptosis (Hoechst 33342++/sytox green+) occurred with the addition of Gd-TP/GQD-RGD (Figure 3, white arrows), indicating the toxicity of the biological redox drug to cancer cells. Cells were mostly apoptotic and some of them were even necrotic (Hoechst 33342++/sytox green++) when Lu-TP/GQD-RGD was imported, which indicates the activation of the PS by light. Moreover, most of the irradiated cells that underwent Lu-TP&Gd-TP/GQD-RGD treatment were necrotic (Figure 3,
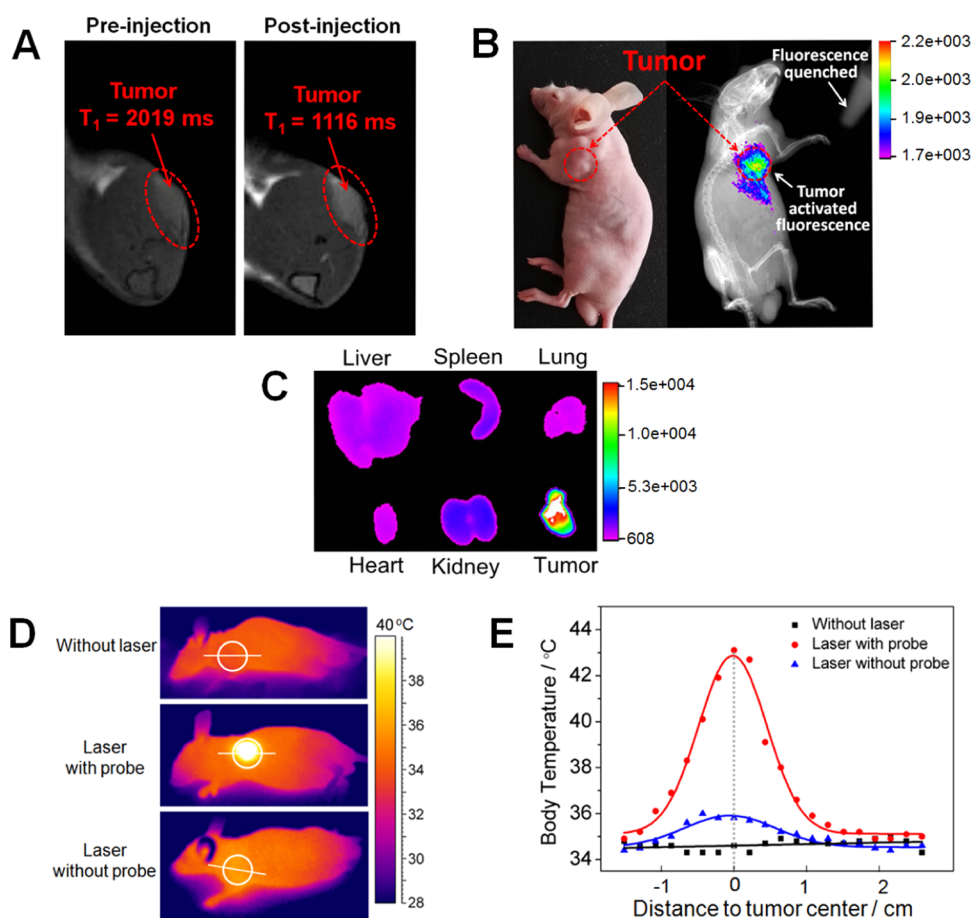
Figure 6. (A) T_1-weighted MRI and (B) fluorescence image of A549 tumor-bearing mice 1.5 h after intravenous injection of Lu-TP&Gd-TP/GQD-RGD. (C) Ex vivo fluorescence imaging of major normal organs and tumor tissue from mice treated with Lu-TP&Gd-TP/GQD-RGD. (D) Thermal images and (E) temperature distribution of GQD-RGD-injected mice after 20 min of irradiation with a 765 nm laser at 300 mW/cm^2.

yellow arrows). Accurate apoptosis and necrosis rates were measured by Annexin V-FITC/PI apoptosis assay. As shown in Figure 4, over 62% of the Lu-TP&Gd-TP/GQD-RGD treated cells were apoptotic or necrotic 10 h after irradiation, in comparison with 3, 17, and 38% for the GQD-RGD, Gd-TP/GQD-RGD, and Lu-TP/GQD-RGD treated cells, respectively. Under the same conditions, MTT results showed that the viability of GQD-RGD, Gd-TP/GQD-RGD, Lu-TP/GQD-RGD, and Lu-TP&Gd-TP/GQD-RGD treated cells were 98.28, 86.59, 68.08, and 37.91%, respectively (Figure S-13). These results further corroborate the hypothesis that the introduction of the redox active drug Gd-TP promotes the apoptosis and/or necrosis of cancer cells in PDT.

To fabricate a smart vehicle that could identify non-small cell lung carcinoma A549 cells, we conjugated the targeting peptide RGD to the GQDs through a PEG bridge. RGD-GQD could be internalized via endocytosis mediated by the $\alpha_v\beta_3$ receptor. $\alpha_v\beta_3$-Positive A549 and $\alpha_v\beta_3$-negative MCF7 breast cancer cells were introduced to study the selectivity of the nanoconstruct. The two types of cells were labeled with red or green emission dyes respectively, and then treated with Lu-TP&Gd-TP/GQD-RGD, followed by a 4 min irradiation period. The red-labeled A549 cells disappeared within the laser footprint (Figure 5), whereas the green-emitting MCF7 cells continued to be visible. These results confirmed the selectivity of Lu-TP&Gd-TP/GQD-RGD toward the A549 cells. Next, we investigated their targeting ability in a cell mixture. In the irradiated region, red-

labeled A549 cells were depleted, whereas green-emitting MCF7 cells remained attached to the substrate. This further demonstrated the high selectivity of the designed nanostructure.

Visualizing the Tumor Site by MRI and Fluorescence Imaging. To evaluate the in vivo imaging potential, we performed MRI scans on A549 tumor-bearing mice intravenously injected with Lu-TP&Gd-TP/GQD-RGD. Owing to the paramagnetic property of Gd(III), the nanoconstruct shortens the T_1 of water protons and acts as a T_1-weighted MRI contrast agent. After 1.5 h post-injection, the proton T_1 was significantly shortened from 2019 to 1106 ms and T_1-weighted images yielded an unambiguous positive contrast, as shown in Figure 6A. This demonstrates the unique potential of the nanoconstruct as a targeting contrast agent for T_1-weighted MRI. Figure 6B shows the in vivo biodistribution profile and tumor accumulation of Lu-TP&Gd-TP/GQD-RGD in A549 tumor-bearing mice. Activated fluorescence (780 nm) in the tumor area was observed after 1.5 h post-injection, which was consistent with the MRI results. Figure 6C shows an ex vivo fluorescence image of various organs and tissues. Obvious fluorescent signal is only observed in the tumor, whereas there is almost no detectable fluorescence originating from the other tissues. These results suggest that Lu-TP&Gd-TP/GQD-RGD remains in the quenched state within normal tissues, whereas in the tumor microenvironment, the fluorescence is active.

Photothermal Effect of GQDs. Carbon-based materials have successfully been used in PTT because they can generate heat from NIR light absorption. As a single-atom-thick layer of sp^2-hybridized carbon atoms, GQDs may also have potential as a photothermal agent. We first tested their photothermal effect in aqueous solution. In contrast to water, a 1 mg/mL GQD aqueous solution showed a rapid response under a low-power 765 nm laser of 300 mW/cm^2 (Figure S-14). After 30 min of irradiation, the temperature of the GQDs in aqueous solution increased from 26.5 to 39.7 °C, which was almost 30 times larger than that of water. We also investigated their ability for heat generation under the same conditions in cell PDT experiments. After 5 min of irradiation at a lower power of 50 mW/cm^2, only a small (1.5 °C) increase in temperature could be detected (Figure S-15). This explains the interesting results from Figure 2. After irradiation, fluorescence from the nanoconstruct was obviously brighter within the laser footprint, because more probes could be delivered as a result of the mild heating. We also directly tested the fluorescence intensity of the probe-incubated cells with and without laser irradiation (Figure S-16). For all five samples, no significant differences in DAPI emission were observed throughout the CLSM images, whereas fluorescence from the probe was 6 times stronger in the irradiated area than that in the unirradiated area. This demonstrated that the probe concentration was higher in the laser areas; thus, the light-induced mild hyperthermia promoted cell uptake of the probe. Next, we examined the in vivo photothermal properties. A549 tumor-bearing mice were intravenously injected with GQD-RGD. After 20 min of irradiation at a power of 300 mW/cm^2, the tumor temperature increased to 43 °C (Figure 6D,E). Conversely, tumors in mice that had not been injected with GQD-RGD remained below 36 °C. Such mild local heating, in contrast to the behavior of other graphene-based materials, promotes probe uptake rather than killing cells directly.

Visualizing the Multitherapy-Induced Tumor Decrease in Vivo. Encouraged by these results showing good PDT efficiency, effective targeting, as well as acceleration of probe uptake, we evaluated the in vivo effect of simultaneous BRT/PTT/PDT. Owing to the accumulated Gd(III), tumor size could be accurately monitored by T$_1$-weighted MRI. For those without a paramagnetic contrast agent, 100 μM/kg Gd−DTPA was injected before the MRI experiments. Groups treated with Lu-TP/GQD-RGD, Gd-TP/GQD-RGD, or Lu-TP&Gd-TP/GQD-RGD showed delayed growth compared with that of the saline-injected group (Figure 7A). In the third week, all A549 tumor-bearing mice in the saline-injected group died. However, all mice in the drug-treated groups remained alive after four weeks. The antitumor effect was monitored by MRI over a period of 21 days. The volumes of the A549 tumors were significantly reduced after BRT−PDT−PTT at day 10. The exact tumor variation over time could be clearly seen via T$_1$-weighted MRI. With low-power laser irradiation at 765 nm, the tumor volume of the Lu-TP&Gd-TP/GQD-RGD treated group decreased to 74% after treatment, in comparison with increased tumor volumes of the Gd-TP/GQD-RGD group (516%), Lu-TP&Gd-TP/GQD-RGD group (183%), and blank group (819%), showing a superior synergistic therapeutic effect. A control group, injected with Lu-TP&Gd-TP/GQD-RGD but not irradiated, showed faster tumor growth than that of the other three groups. After three periods of treatment, the best therapeutic effect of Lu-TP&Gd-TP/GQD-RGD could be intuitively visualized by the MRI results (Figure 7B). The
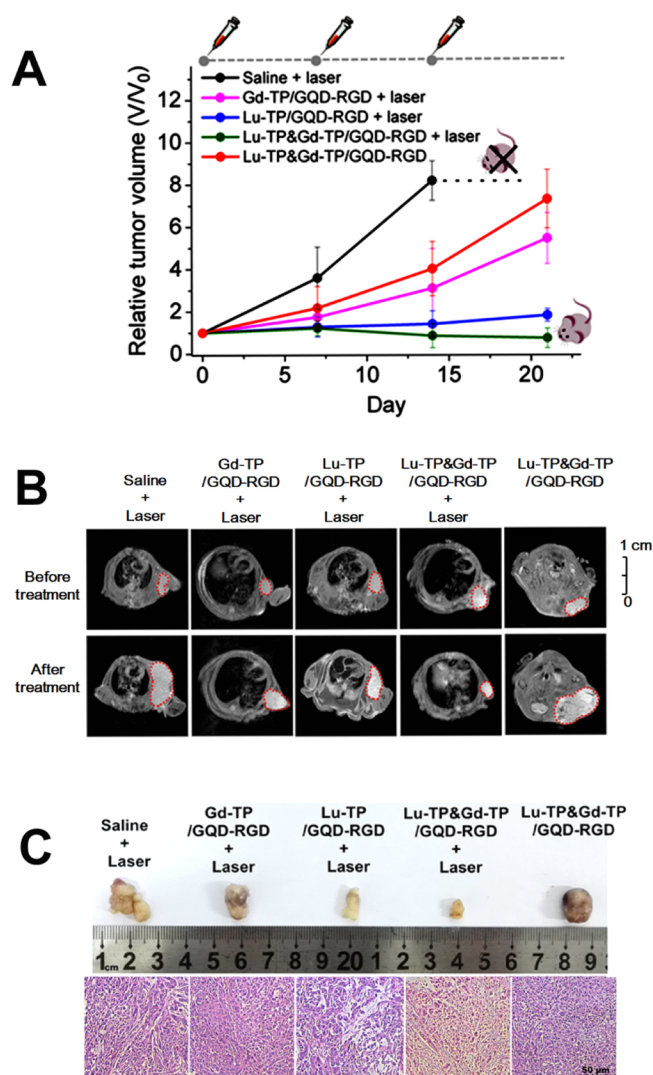

Figure 7. Evaluation of in vivo therapeutic efficacy in a subcutaneous tumor model. (A) Tumor growth curves as a function of time after treatment. The tumor sites were irradiated for 20 min with a 765 nm laser (300 mW/cm^2) 1.5 h post-injection of Gd-TP/GQD-RGD, Lu-TP/GQD-RGD, or Lu-TP&Gd-TP/GQD-RGD. Tumor sizes were measured before treatment and the tumor volumes were normalized to their initial sizes. (B) Antitumor efficiency on A549-implanted mice model assessed by MRI. Tumors before and after three periods of treatment are marked by the red dotted line. (C) Photos and representative histopathological results of the excised tumors after treatment with Gd-TP/GQD-RGD, Lu-TP/GQD-RGD, Lu-TP&Gd-TP/GQD-RGD, or saline. Scale bar, 50 μm.

treatment efficiency was also evaluated by H&E staining assay. Prominent necrosis was observed in the tumor tissues of the group treated with Lu-TP&Gd-TP/GQD-RGD and irradiation, whereas no apparent necrosis was found in the other four groups (Figure 7C). The in vivo toxicity of the designed system was also estimated. GQD-RGD and Lu-TP&Gd-TP/GQD-RGD in a series of concentrations from 25 to 200 μg/mL had a hemolysis rate lower than 5% by turbidimetric assay with human red blood cells (Figure S-17). Furthermore, the designed therapeutic strategy did not show any damage to the liver, kidney, and spleen, indicating its low toxicity to normal tissues (Figure S-18). The stable weight of the animals in the model during treatment also suggested negligible influence of the designed drugs on them (Figure S-19).

■ CONCLUSIONS

In this work, GQDs were used as a multifunctional nanocarrier to load Gd-TP and Lu-TP for BRT-enhanced PDT and PTT. The biological redox enhancement by Gd-TP dramatically increases the PDT efficiency of Lu-TP, producing immediate cancer cell death at very low doses of PDT. Further combining this method with the light-triggered mild PTT of GQDs improves the biological redox-enhanced PDT efficacy remarkably. The nanoconstruct also exhibits tumor-responsive deep-red fluorescence and enhanced T1-weighted MRI that enable imaging of the tumor during treatment. This new hybrid nanosystem provides a powerful new multimodal tool for the treatment and imaging of cancer.

■ EXPERIMENTAL SECTION

Materials. MCNTs were purchased from Nanjing XFNANO Materials Tech Co., Ltd (Nanjing, China). Gadolinium(III) chloride hexahydrate ($GdCl_3·6H_2O$, 99%), lutetium(III) nitrate hydrate ($Lu(NO_3)_3·xH_2O$), and poly(ethylene glycol) bis(amine) (PEG-diamine, M_r 2000) were purchased from Sigma-Aldrich (St. Louis). c(RGDyK) was purchased from GL Biochem (Shanghai, China). Dialysis bags (M_r 3500 Da) were purchased from Biosharp (Hefei, China). Human lung adenocarcinoma cell line A549 and breast cancer cell line MCF7 were obtained from the Cell Bank of Chinese Academy of Sciences (Shanghai, China).

Synthesis of GQDs. A two-step approach was employed to fabricate orange-emitting GQDs. First, MWCNTs (50 mg) were suspended in a mixture of 98% sulfuric acid (50 mL), fuming nitric acid (15 mL), and distilled water (5 mL) by sonication. After 24 h of heating at 70 °C, the mixture was cooled to room temperature and diluted with 250 mL of DI water. The obtained solution was neutralized by Na_2CO_3 and then filtrated to remove the precipitated salt. Redundant salt was removed by dialysis against distilled water, and the obtained solution was evaporated to 50 mL and lyophilized. Second, the oxidized MCNTs were cut into GQDs by a microwave-assisted hydrothermal method. The obtained brown powder was dispersed in DMF by 30 min of sonication (120 W, 100 kHz). Of the mixed solution, 6 mL was transferred to an exclusive vitreous vessel with a volume of 10 mL. Orange-emitting GQDs were prepared at 200 °C for 20 min. After cooling to room temperature, the obtained mixture was filtered through a 0.22 μm microporous filter. A brown solution was obtained by washing the used microporous filter with distilled water. Large fragments were eliminated by filtering the solution with a 0.02 μm anopore inorganic membrane (AnodiscTM, Watman). To further remove the DMF residues, the obtained GQD aqueous solution was further dialyzed for 48 h in high purity water.

Synthesis of GQD-RGD. 191 mg of EDCI·HCl and 10 mg of GQDs were placed in a 50 mL round-bottom flask with 10 mL of distilled water. The pH was adjusted to 5.0 by 0.1 mM HCl. After 10 min of sonication and 2 h of stirring at room temperature, the pH was then adjusted to 8.0 by 0.1 mM NaOH. Then, 28.75 mg of NHS and 50 mg of EtO-PEG-NH₂ in 10 mL of DMF was added. The mixture was stirred for another 24 h at room temperature. The produced GQD-PEG-OEt solution was purified by dialysis against distilled water. To hydrolyze the ester group, 2.5 mg of KOH was added to a mixture of distilled water and methanol (1:1) solution that dispersed the freeze-dried GQD-PEG-OEt. After being left to react overnight, excess small molecules were removed by dialysis. RGD was further attached to the GQDs by an acylation reaction between the carboxyl groups of GQD-PEG-COOH and the amino groups of RGD.

Loading of Lu-TP and/or Gd-TP on GQD-RGD. GQD-RGD and Lu-texaphyrin and/or Gd-texaphyrin were mixed in a distilled water/ DMSO solution by sonication, and the mixture was further stirred overnight in the dark at room temperature. The obtained mixture was dialyzed against DI water to remove free DMSO. Unbound Lu-texaphyrin and/or Gd-texaphyrin was dislodged by centrifugation at 5000 rpm for 3 min. Concentration of the formed Lu-TP&Gd-TP/ GQD-RGD complex solution was carried out by ultrafiltration in an

ultracentrifugal filter (Millipore, 3 K) at 5000 rpm for 20 min. The resulting Lu-TP&Gd-TP/GQD-RGD aqueous solution was preserved in darkness at 4 °C.

Cellular Uptake of Lu-TP&Gd-TP/GQD-RGD and PDT. A549 cells were maintained in DMEM medium, supplemented with 10% inactivated fetal bovine serum and 1% penicillin/streptomycin 10 000 U/mL, and were grown in an incubator at 37 °C, supplied with 5% CO_2. For the cellular uptake of the designed nanoprobe, A549 cells at a density of 2×10^6/mL were seeded in a six-well chamber slide with one piece of cover glass at the bottom of each chamber. After 12 h of plating, solutions of GQD-RGD, Gd-TP/GQD-RGD, Lu-TP/GQD-RGD, and Lu-TP&Gd-TP/GQD-RGD were added, respectively. After 4 h of incubation, the cells were irradiated using a 765 nm laser at a power density of 50 mW/cm² for 4 min. Then, the cells were washed with PBS 7.4 three times to remove extra solution. The cells were further incubated in cell medium DMEM at 37 °C for 24 h. To achieve fixation, cells were immersed in 4% paraformaldehyde in PBS for 10 min at room temperature. Following fixation, the slides were washed three times with distilled water and visualized under a laser scanning confocal microscope, Nikon A1.

In Vivo MRI. Imaging was performed on a 7 T, small-animal horizontal bore system (Bruker BioSpec; Bruker, Billerica, MA). A 12 cm diameter Helmholtz coil arrangement was used for rf excitation, whereas signal detection was achieved with a 23-mm diameter surface coil. The coils were decoupled from each other. Gradients used in the magnet were 12 cm in diameter at 25 G/cm. Imaging was performed using a custom-built 50 mm in diameter send−receive birdcage volume coil. Following anesthesia of the mice using 4% isoflurane/ oxygen, mice were fixed to an acrylic patient bed in the prone position and maintained on a 1% isoflurane/oxygen mixture. Body temperature was monitored with a platinum rectal probe connected to a small-animal monitoring system (SA Incorporated) and maintained using a stream of heated air. T_1-weighted images were acquired in the axial plane using a multislice spin-echo sequence with the following parameters: TR/TE = 400/11 ms, matrix = 128 × 128, field of view = 30 mm × 30 mm, slice thickness = 1 mm, number of excitations = 4. Scans were completed before and after intravenous injection of Lu-TP&Gd-TP/GQD-RGD aqueous solution via the tail vein.

In Vivo Fluorescence Imaging. Lu-TP&Gd-TP/GQD-RGD aqueous solution was intravenously injected via the tail vein after the nude mice were anesthetized by peritoneal injection of pelltobarbitalum natricum at a concentration of 50 mg/kg. The mice were then transferred into a Bruker imaging system, and a laser of 710 nm was applied to excite the probe. Fluorescence imaging photographs were acquired every 10 min to monitor the location of the injected probe.

In Vivo PDT. To evaluate the in vivo PDT efficiency, probes were intravenously injected into nude mice with a tumor of ∼5 mm via the tail vein. At 1.5 h post-injection, the mice were anesthetized by peritoneal injection of pelltobarbitalum natricum and the tumor area was irradiated with a 765 nm laser for 20 min. The laser power was measured to be 300 mW with a spot size of 1 cm in diameter.

A549 tumor-bearing mice were divided into six groups of five animals per group to quantify the growth rate of the tumors after the following treatments: (i) physiological saline administrated and irradiated; (ii) Gd-TP/GQD-RGD aqueous solution administrated and irradiated; (iii) Lu-TP/GQD-RGD aqueous solution administrated and irradiated; (iv) Lu-TP&Gd-TP/GQD-RGD aqueous solution administrated, no irradiation; (v) Lu-TP&Gd-TP/GQD-RGD aqueous solution administrated and irradiated. The mice were treated every seventh day, and all groups were treated for three periods.

Tumor size was measured by MRI before treatment. The volume of a tumor (V) was calculated by the following equation: $V = A \times B \times C$, where A and B are the length and width (mm) of the tumor, respectively, which could be accurately calculated from the maximum transverse section of the tumor across the MRI scans. C is the height of the tumor, which was estimated from the number of MRI slices containing the tumor.

ASSOCIATED CONTENT

Ⓢ Supporting Information

The Supporting Information is available free of charge on the ACS Publications website at DOI: 10.1021/acsami.7b05463.

Detailed synthetic protocols of texaphyrin and EtO-PEG-NH$_2$, mass spectra of the synthesized drugs, UV and photoluminescence spectra, detection of ROS generation, cellular selectivity, apoptosis experiments, Annexin V-FITC/PI apoptosis detection, in vitro and in vivo treatments (PDF)

AUTHOR INFORMATION

Corresponding Author

*E-mail: xinzhou@wipm.ac.cn.

ORCID Ⓘ

Louis-S. Bouchard: 0000-0003-4151-5628
Xin Zhou: 0000-0002-5580-7907

Author Contributions

§Y.Y. and S.C. contributed equally to this work.

Notes

The authors declare no competing financial interest.

ACKNOWLEDGMENTS

REFERENCES

(1) Ferrari, M. Cancer Nanotechnology: Opportunities and Challenges. *Nat. Rev. Cancer* **2005**, *5*, 161−171.

(2) Trachootham, D.; Alexandre, J.; Huang, P. Targeting Cancer Cells by ROS-Mediated Mechanisms: A Radical Therapeutic Approach? *Nat. Rev. Drug Discovery* **2009**, *8*, 579−591.

(3) Dolmans, D. E.; Fukumura, D.; Jain, R. K. Photodynamic Therapy for Cancer. *Nat. Rev. Cancer* **2003**, *3*, 380−387.

(4) Castano, A. P.; Mroz, P.; Hamblin, M. R. Photodynamic Therapy and Anti-tumour Immunity. *Nat. Rev. Cancer* **2006**, *6*, 535−545.

(5) Fan, W.; Huang, P.; Chen, X. Overcoming the Achilles' Heel of Photodynamic Therapy. *Chem. Soc. Rev.* **2016**, *45*, 6488−6519.

(6) Chang, J. H.; Gabison, E. E.; Kato, T.; Azar, D. T. Corneal Neovascularization. *Curr. Opin. Ophthalmol.* **2001**, *12*, 242−249.

(7) Preston, D. S.; Stern, R. S. Nonmelanoma Cancers of the Skin. *N. Engl. J. Med.* **1992**, *327*, 1649−1662.

(8) Hayata, Y.; Kato, H.; Konaka, C.; Okunaka, T. Photodynamic Therapy (PDT) in Early Stage Lung Cancer. *Lung Cancer* **1993**, *9*, 287−293.

(9) Blumenkranz, M. S.; Woodburn, K. W.; Qing, F.; Verdooner, S.; Kessel, D.; Miller, R. Lutetium Texaphyrin (Lu-Tex): A Potential New Agent for Ocular Fundus Angiography and Photodynamic Therapy. *Am. J. Ophthalmol.* **2000**, *129*, 353−362.

(10) Magda, D.; Miller, R. A. Motexafin Gadolinium: A Novel Redox Active Drug for Cancer Therapy. *Semin. Cancer Biol.* **2006**, *16*, 466−476.

(11) Liu, H.; Chen, D.; Li, L. L.; Liu, T. L.; Tan, L. F.; Wu, X. L.; Tang, F. Q. Multifunctional Gold Nanoshells on Silica Nanorattles: A Platform for the Combination of Photothermal Therapy and Chemotherapy with Low Systemic Toxicity. *Angew. Chem., Int. Ed.* **2011**, *50*, 891−895.

(12) Pogue, B. W.; O'Hara, J. A.; Demidenko, E.; Wilmot, C. M.; Goodwin, I. K.; Chen, B.; Swartz, H. M.; Hasan, T. Photodynamic Therapy with Verteporfin in the Radiation-induced Fibrosarcoma-1 Tumor Causes Enhanced Radiation Sensitivity. *Cancer Res.* **2003**, *63*, 1025−1033.

(13) Pass, H. I.; Temeck, B. K.; Kranda, K.; Gunthe, T.; Russo, A.; Smith, P.; Friauf, W.; Steinberg, S. M. Phase III Randomized Trial of Surgery with or without Intraoperative Photodynamic Therapy and Postoperative Immunochemotherapy for Malignant Pleural Mesothelioma. *Ann. Surg. Oncol.* **1997**, *4*, 628−633.

(14) Wang, X.; Li, X.; Ito, A.; Watanabe, Y.; Sogo, Y.; Tsuji, N. M.; Ohno, T. Stimulation of In Vivo Antitumor Immunity with Hollow Mesoporous Silica Nanospheres. *Angew. Chem., Int. Ed.* **2016**, *55*, 1899−1903.

(15) Liang, X. L.; Li, Y. Y.; Li, X. D.; Jing, L. J.; Deng, Z. J.; Yue, X. L.; Li, C. H.; Dai, Z. F. PEGylated Polypyrrole Nanoparticles Conjugating Gadolinium Chelates for Dual-Modal MRI/Photoacoustic Imaging Guided Photothermal Therapy of Cancer. *Adv. Funct. Mater.* **2015**, *25*, 1451−1462.

(16) Lin, J.; Wang, S.; Huang, P.; Wang, Z.; Chen, S.; Niu, G.; Li, W.; He, J.; Cui, D.; Lu, G.; Chen, X.; Nie, Z. Photosensitizer-Loaded Gold Vesicles with Strong Plasmonic Coupling Effect for Imaging-Guided Photothermal/Photodynamic Therapy. *ACS Nano* **2013**, *7*, 5320−5329.

(17) Fang, S.; Lin, J.; Li, C.; Huang, P.; Hou, W.; Zhang, C.; Liu, J.; Huang, S.; Luo, Y.; Fan, W.; Cui, D.; Xu, Y.; Li, Z. Dual-Stimuli Responsive Nanotheranostics for Multimodal Imaging Guided Trimodal Synergistic Therapy. *Small* **2017**, *13*, No. 1602580.

(18) Mura, S.; Nicolas, J.; Couvreur, P. Stimuli-responsive Nanocarriers for Drug Delivery. *Nat. Mater.* **2013**, *12*, 991−1003.

(19) Tang, L.; Ji, R. B.; Li, X. M.; Bai, G. X.; Liu, C. P.; Hao, J. H.; Lin, J. Y.; Jiang, H. X.; Teng, K. S.; Yang, Z. B.; Lau, S. P. Deep Ultraviolet to Near-Infrared Emission and Photoresponse in Layered N-Doped Graphene Quantum Dots. *ACS Nano* **2014**, *8*, 6312−6320.

(20) Xie, J.; Chen, K.; Lee, H. Y.; Xu, C.; Hsu, A.; Peng, S.; Chen, X. Y.; Sun, S. H. Ultrasmall c(RGDyK)-coated Fe$_3$O$_4$ Nanoparticles and Their Specific Targeting to Integrin $\alpha_v\beta_3$-rich Tumor Cells. *J. Am. Chem. Soc.* **2008**, *130*, 7542−7543.

(21) Sherlock, S. P.; Tabakman, S. M.; Xie, L. M.; Dai, H. J. Photothermally Enhanced Drug Delivery by Ultrasmall Multifunctional FeCo/Graphitic Shell Nanocrystals. *ACS Nano* **2011**, *5*, 1505−1512.

(22) Bouchard, L. S.; Anwar, M. S.; Liu, G. L.; Hann, B.; Xie, Z. H.; Gray, J. W.; Wang, X. D.; Pines, A.; Chen, F. F. Picomolar Sensitivity MRI and Photoacoustic Imaging of Cobalt Nanoparticles. *Proc. Natl. Acad. Sci. U.S.A.* **2009**, *106*, 4085−4089.

(23) Santra, S.; Jativa, S. D.; Kaittanis, C.; Normand, G.; Grimm, J.; Perez, J. M. Gadolinium-Encapsulating Iron Oxide Nanoprobe as Activatable NMR/MRI Contrast Agent. *ACS Nano* **2012**, *6*, 7281−7294.

(24) Peng, J.; Gao, W.; Gupta, B. K.; Liu, Z.; Romero-Aburto, R.; Ge, L. H.; Song, L.; Alemany, L. B.; Zhan, X. B.; Gao, G. H.; Vithayathil, S. A.; Kaipparettu, B. A.; Marti, A. A.; Hayashi, T.; Zhu, J. J.; Ajayan, P. M. Graphene Quantum Dots Derived from Carbon Fibers. *Nano Lett.* **2012**, *12*, 844−849.

(25) Liu, Q.; Guo, B. D.; Rao, Z. Y.; Zhang, B. H.; Gong, J. R. Strong Two-Photon-Induced Fluorescence from Photostable, Biocompatible Nitrogen-Doped Graphene Quantum Dots for Cellular and Deep-Tissue Imaging. *Nano Lett.* **2013**, *13*, 2436−2441.

(26) Grossweiner, L. I.; Bilgin, M. D.; Berdusis, P.; Mody, T. D. Singlet Oxygen Generation by Metallotexaphyrins. *Photochem. Photobiol.* **1999**, *70*, 138−145.